

# Kinematics of the Nuclear Ionized Gas in the Radio Galaxy M84 (NGC 4374)<sup>1</sup>

G. A. Bower<sup>2</sup>, R. F. Green<sup>2</sup>, A. Danks<sup>3</sup>, T. Gull<sup>4</sup>, S. Heap<sup>4</sup>, J. Hutchings<sup>5</sup>, C. Joseph<sup>6</sup>, M. E. Kaiser<sup>4,7</sup>, R. Kimble<sup>4</sup>, S. Kraemer<sup>8</sup>, D. Weistrop<sup>9</sup>, B. Woodgate<sup>4</sup>, D. Lindler<sup>10</sup>, R. S. Hill<sup>3</sup>, E. M. Malumuth<sup>3</sup>, S. Baum<sup>11</sup>, V. Sarajedini<sup>12</sup>, T. M. Heckman<sup>7,11</sup>, A. S. Wilson<sup>11,13</sup>, and D. O. Richstone<sup>14</sup>

To appear in the *Astrophysical Journal Letters*

---

<sup>1</sup>Based on observations with the NASA/ESA *Hubble Space Telescope*, obtained at the Space Telescope Science Institute, which is operated by the Association of Universities for Research in Astronomy, Inc. (AURA), under NASA contract NAS5-26555.

<sup>2</sup>Kitt Peak National Observatory, National Optical Astronomy Observatories, P. O. Box 26732, Tucson, AZ 85726

<sup>3</sup>Hughes/STX, NASA/Goddard Space Flight Center, Code 681, Greenbelt, MD 20771

<sup>4</sup>NASA/Goddard Space Flight Center, Code 681, Greenbelt, MD 20771

<sup>5</sup>Dominion Astrophysical Observatory, National Research Council of Canada, 5071 W. Saanich Road, Victoria, BC V8X 4M6, Canada

<sup>6</sup>Dept. of Physics & Astronomy, Rutgers University, P. O. Box 849, Piscataway, NJ 08855

<sup>7</sup>Department of Physics & Astronomy, Johns Hopkins University, Homewood Campus, Baltimore, MD 21218

<sup>8</sup>Catholic University, Department of Physics, NASA/Goddard Space Flight Center, Code 681, Greenbelt, MD 20771

<sup>9</sup>Department of Physics, University of Nevada, 4505 S. Maryland Parkway, Las Vegas, NV 89154

<sup>10</sup>Advanced Computer Concepts, Inc., NASA/Goddard Space Flight Center, Code 681, Greenbelt, MD 20771

<sup>11</sup>Space Telescope Science Institute, 3700 San Martin Drive, Baltimore, MD 21218

<sup>12</sup>Steward Observatory, University of Arizona, Tucson, AZ 85721

<sup>13</sup>Astronomy Department, University of Maryland, College Park, MD 20742

<sup>14</sup>Department of Astronomy, University of Michigan, Dennison Building, Ann Arbor, MI 48109

## ABSTRACT

We present optical long-slit spectroscopy of the nucleus of the nearby radio galaxy M84 (NGC 4374 = 3C 272.1) obtained with the Space Telescope Imaging Spectrograph (STIS) aboard the *Hubble Space Telescope* (HST). Our spectra reveal that the nuclear gas disk seen in WFPC2 imaging by Bower et al. (1997, ApJ, 483, L33) is rotating rapidly. The velocity curve has an S-shape with a peak amplitude of  $400 \text{ km s}^{-1}$  at  $0''.1 = 8 \text{ pc}$  from the nucleus. To model the observed gas kinematics, we construct a thin Keplerian disk model that fits the data well if the rotation axis of the gas disk is aligned with the radio jet axis. These models indicate that the gas dynamics are driven by a nuclear compact mass of  $1.5 \times 10^9 M_{\odot}$  with an uncertainty range of  $(0.9 - 2.6) \times 10^9 M_{\odot}$  and that the inclination of the disk with respect to the plane of the sky is  $75^{\circ} - 85^{\circ}$ . Of this nuclear mass, only  $\leq 2 \times 10^7 M_{\odot}$  can possibly be attributed to luminous mass. Thus, we conclude that a dark compact mass (most likely a supermassive black hole) resides in the nucleus of M84.

*Subject headings:* galaxies: active — galaxies: elliptical and lenticular, cD — galaxies: individual (M84) — galaxies: kinematics and dynamics — galaxies: nuclei

## 1. Introduction

M84 is an E1 galaxy in the Virgo Cluster with an active galactic nucleus and hosts the F-R I (Fanaroff & Riley 1974) radio source 3C 272.1. Bower et al. (1997; hereafter Paper I) obtained images of M84 with the Wide Field/Planetary Camera 2 (WFPC2) aboard HST, showing that the ionized gas within the central kpc has three components: a nuclear gas disk, outer filaments, and an ‘ionization cone’. The nuclear gas disk has diameter  $\approx 1''$  (82 pc) and a major axis P.A.  $\approx 58^\circ$  that is tilted by  $\approx 25^\circ$  with respect to the major axis P.A. of the outer filamentary emission. This outer filamentary emission had been seen in ground-based imaging (e.g., Hansen et al. 1985; Baum et al. 1988). Its major axis is approximately perpendicular to the axis of the radio jets (Laing & Bridle 1987; Jones et al. 1981).

The presence of a nuclear gas disk in M84 is especially interesting. If the gas exhibits Keplerian motion about the nucleus, then a straightforward application of Newton’s laws to the dynamics of this gas disk would provide an estimate of the mass of the putative supermassive black hole (BH) in M84’s nucleus. It is plausible that M84 contains a BH, since it is a radio galaxy and the rotation gradient of the ionized gas is spatially unresolved (i.e.,  $> 100 \text{ km s}^{-1} \text{ arcsec}^{-1}$ ) in ground-based observations (Baum et al. 1990, 1992). Previous HST observations using the Faint Object Spectrograph have found gas-dynamical evidence for BHs in other galaxies containing nuclear gas disks, such as M87 and NGC 4261 (Harms et al. 1994; Ferrarese et al. 1996). STIS (through the use of a CCD in a long-slit spectrograph) provides a significant improvement in HST’s efficiency for measuring the nuclear dynamics of galaxies. We chose M84 as a target for a demonstration.

In this paper, we analyze the dynamics of the nuclear gas disk in M84 to probe the nuclear gravitational potential. The analysis of gas dynamics in galactic nuclei is complementary to the method of analyzing the stellar dynamics (e.g., Kormendy et al. 1996). However, measuring the stellar kinematics in M84 using HST would be challenging, since the stellar surface brightness at the nucleus (determined from the WFPC2 F547M image in Paper I) is rather modest ( $\mu_V \approx 16 \text{ mag arcsec}^{-2}$ ). For M84, the gas kinematics are far easier to measure than the stellar kinematics given the high surface brightness in the emission lines.

Throughout this paper, we adopt a distance to M84 of 17 Mpc (Mould et al. 1995). At this distance,  $1''$  corresponds to 82 pc. The Galactic extinction along the line of sight is  $A_B = 0^m13$  (Burstein & Heiles 1984).

## 2. Observations and Data Calibration

Long-slit spectroscopy of M84’s nuclear region was obtained with the STIS CCD, which has a pixel scale of  $0''.05/\text{pixel}$  (Baum et al. 1996), aboard HST on 1997 April 14 and 17 with the telescope tracking in fine lock with one FGS probe (nominal jitter  $\approx 0''.007$ ). Since M84’s nucleus contains a bright optical point source (Paper I), the nucleus was acquired easily to an accuracy of  $0''.05$  by the ACQ mode using two iterations of two 10 sec imaging exposures through the F28X50LP optical long-pass filter. The ACQ/PEAK mode (Baum et al. 1996) was not available during these observations since they were obtained early during Servicing Mission Orbital Verification (SMOV). The  $52'' \times 0''.2$  slit was aligned at a position angle (P.A.) of  $104^\circ$ . This was the closest that the slit could be aligned with the gas disk’s major axis (P.A. =  $58^\circ$ ; Paper I) because of HST scheduling constraints during SMOV. To allow for the centering accuracy of only  $0''.05$  and for the offset between the slit P.A. and the gas disk’s major axis, we planned to obtain spectra at four different slit positions offset from the nucleus by  $-0''.3$ ,  $-0''.1$ ,  $+0''.1$ , and  $+0''.3$ , where the offsets were perpendicular to the slit and negative spatial offsets moved the slit toward a P.A. of  $14^\circ$  on the sky. However, below we discuss an empirical determination of the slit positions using our STIS data and the WFPC2 images from Paper I, showing that the actual offsets were  $-0''.2$ ,  $0''.0$ ,  $+0''.2$ , and  $0''.0$ . For the fourth offset position, the discrepancy between the planned and actual positions occurred because this last spectrum was obtained during the second visit of M84, with an erroneously commanded offset. This error was fortuitous because from our analysis below it is apparent that the kinematic signature of the nuclear gas disk is readily detectable only within  $\sim 0''.3$  of the nucleus, beyond which the kinematics of the outer filamentary emission (which do not necessarily provide good leverage on the nuclear gravitational potential) dominates the spectrum.

At each slit position, we obtained spectra with the G750M grating, which has a dispersion of  $0.56 \text{ \AA}/\text{pixel}$ . This grating was set to cover the wavelength range of  $6295 \text{ \AA}$  to  $6867 \text{ \AA}$ , which includes the emission lines of  $\text{H}\alpha$ ,  $[\text{N II}] \lambda\lambda 6548, 6583$ , and  $[\text{S II}] \lambda\lambda 6717, 6731$ . The spectral resolution of our instrumental configuration was  $2.2 \text{ \AA} \approx 100 \text{ km s}^{-1}$  (FWHM), assuming uniform illumination of the slit. However, Paper I shows that at the nucleus, there is a point source in the optical continuum, and the  $\text{H}\alpha + [\text{N II}]$  emission is very compact. Thus, our spectral resolution at the nucleus was better than  $100 \text{ km s}^{-1}$ . We integrated for two HST orbits at each slit position, which was equivalent to  $4500 - 5100$  sec per slit position depending on the occurrence of instrumental overheads. Spectra of the internal wavelength calibration source (wavecals) were interspersed among the galaxy spectra to allow for correction of thermal drifts during data reduction.

The data were calibrated using the CALSTIS pipeline to perform the steps of bias

subtraction, dark subtraction, applying the flatfield, and combining the two sub-exposures to reject cosmic-ray events. The accuracy of the flatfield calibration was 1%. To reject hot pixels from the data, we employed dark frames obtained immediately before and after the M84 observations. We examined the input data, the flagged hot pixels, and the cleaned output data to ensure that only hot pixels were rejected. The data were wavelength calibrated and rectified by tracing the wavecalcs (using the Ne emission lines for the dispersion axis and the shadows of the two occulting bars for the spatial axis) and then applying these solutions for the geometric distortions to the data. The largest offset that we found between the actual and nominal dispersion solutions was 0.30 pixels, which is significant given that the dispersion solutions were accurate to 0.06 pixels ( $0.03 \text{ \AA} = 1 \text{ km s}^{-1}$ ). The data were then rebinned onto a  $\log \lambda$  scale with a reciprocal dispersion of  $25 \text{ km s}^{-1} \text{ pixel}^{-1}$ .

At this point, we measured the slit positions implied by comparing the flux along the slit with the WFPC2 images from Paper I. Since the on-orbit flux calibration for our grating tilt was not known accurately at the time of our analysis, we normalized the spectra by the observed continuum intensity distribution. The predicted continuum normalized WFPC2 F658N fluxes were then determined by using the STSDAS task “synphot” on the normalized STIS spectra. These predictions were compared with the WFPC2 F658N image normalized by the synthetic  $6590 \text{ \AA}$  continuum image (constructed from the F547M and F814W images; see Paper I for details), indicating that the actual slit positions were offset by  $-0''.2$ ,  $0''.0$ ,  $+0''.2$ , and  $0''.0$  (shown in Fig. 1). However, the uncertainty is as high as  $\pm 0''.1$  since the nuclear gas disk is very compact (Paper I) and the slit width was rather large. These empirical positions are favored because the gas kinematics (measured in §3) are symmetric with respect to the nucleus for these empirical positions. The relative steps between slit positions of  $0''.2$  are assumed to be much more accurate than the absolute placement.

### 3. Measurement of the Gas Kinematics

Fig. 2 shows the last offset =  $0''.0$  spectrum centered on the  $[\text{N II}] \lambda 6583$  emission line. The first iteration at measuring the radial velocities involved cross correlating each spectral row from the four long-slit spectra with a synthetic emission-line spectrum, which included only the five emission lines that we detected in M84 (see Fig. 3) with flux ratios set at values typically found in the data. We then compared the velocities measured by the cross correlation technique with those measured manually from the emission-line peaks. These measurements agree very well for distances  $> 0''.3$  from the nucleus. For rows closer to the nucleus than this, the emission line profiles usually exhibit two kinematic components rather than a single component. These two components are readily seen in the strong

[N II]  $\lambda 6583$  profile (as shown in Fig. 4), especially for the two spectra with offset =  $0''.0$ . Since the velocity measured by our cross correlation technique (using our synthetic template spectrum) coincides with the flux-weighted centroid over a given emission-line profile, these measurements will be distorted when more than one kinematic component is present. We determined which of the [N II]  $\lambda 6583$  profiles in Fig. 4 have two kinematic components by fitting model profiles to a few examples. Separate models with one or two Gaussians were fit to the profiles. If the improvement in  $\chi^2$  was significant, then the profile was classified as having two kinematic components. Although these models were not good fits to the observed profiles (which have broader wings than a Gaussian), this procedure was sufficient for objectively determining which profiles have two components. The velocities for the separate components were then measured by finding the centroid of each component peak.

Based on the  $H\alpha + [N II]$  image (see Fig. 1), it is not surprising that two kinematic components are seen within  $\sim 0''.3$  of the nucleus in the STIS spectroscopy. Paper I identified three spatial components in the ionized gas, including the nuclear gas disk, the outer filaments, and an ionization cone. Given these spatial components, the line of sight to the nuclear gas disk should also intersect the outer filamentary gas (and perhaps the ionization cone) lying in the foreground. Since the outer filamentary gas rotates about the nucleus at  $\approx \pm 100 \text{ km s}^{-1}$  (Baum et al. 1990, 1992), one expects to see this low-velocity component superposed onto the high-velocity kinematics of the nuclear gas disk. Fig. 5 shows our velocity measurements along the slit for each of the four slits. Our measurements of the low-velocity component agree very well with those of Baum et al. (1990). This measurement of the high-velocity component is the first time that the kinematics of M84’s nuclear gas disk have been resolved.

#### 4. Interpretation

The high amplitude and S-shape of the velocity curve in the center of M84 strongly suggest that the emitting gas is in organized motion around a massive central object. To estimate the central mass, numerical models were constructed of a thin Keplerian disk. The continuous velocity sampling along the slit and the two offset slit positions give important constraints on the model parameters.

The models were calculated as follows. By construction,  $V$  (the velocity of gas at any point on the disk) is proportional to  $r^{-1/2}$ , where  $r$  is the distance from the center in the disk plane. The observed velocities were matched by adopting a systemic velocity for the emitting gas. The relative weighting as a function of radius was assumed to follow the major axis isophotal intensity map  $I(r)$  derived in Paper I (i.e.,  $I(r) \propto r^{-1}$ ). To avoid divergence, the

velocity was truncated interior to a selected physical radius at its value at that radius; the intensity weighting was truncated interior to a chosen projected radius at its corresponding value. The disk is inclined to the plane of the sky by an angle  $i$ , and the slit is rotated with respect to the major axis of the disk by an angle  $\theta$ . The slit can also be offset from the nucleus by a specified distance in a direction perpendicular to the slit rotation angle. The contribution to the velocity peak at any sample pixel is weighted by both the projected disk intensity distribution and by the PSF of HST + STIS. The PSF was approximated as a Gaussian with dispersion  $\sigma$ , centered at the midpoint of each sample pixel and integrated to a distance of  $4\sigma$ . Since the  $0''.2$  slit is substantially wider than the FWHM of the delivered PSF, the measured velocity centroid of each pixel sample should be dominated by the effects of the PSF.

The most important free parameter is the mass of the central object. The range of the other parameters is interesting primarily for the extent to which they bound the acceptable range of masses, with one exception to be discussed below. After many realizations of the model, several of the parameters were fixed, either because they were tightly or externally constrained, or because the results were insensitive to reasonable choices. The physical inner radius and the intensity weighting inner radius are examples of the latter case. The PSF is known from both modeling and measurement of standard stars. A Gaussian fit to a model encircled energy curve for HST + STIS + guiding jitter suggested  $\sigma = 0''.06$ . A fit to a short exposure of a standard star observed with the G750M grating produced  $\sigma = 0''.04$ . Those values bracketed the actual width of the velocity inflection of the S-shaped curve. A  $\sigma = 0''.05$  was adopted, corresponding to a FWHM of  $0''.12$ . The fact that the PSF for a longer exposure guided with just one FGS probe appears to be somewhat wider than that for a brief standard star exposure is not unreasonable. The systemic velocity required to symmetrize the peak velocities of the model with respect to the data is  $1125 \text{ km s}^{-1}$ . A variation of  $25 \text{ km s}^{-1}$  in either direction leads to a noticeable degradation in the quality of the fit.

The first approach to determining the central mass was to assume that the isophotal fit of the emission-line intensity in Paper I gave directly the ellipticity and P.A. of the gas disk within  $0''.5$  of the nucleus. Those values are an ellipticity of 0.17, corresponding to  $i = 34^\circ$ , and a P.A. of  $58^\circ$ , leading to a relative slit angle of  $46^\circ$ . No acceptable fit of the zero-offset positions could be produced at  $i = 34^\circ$ . The modeled velocities of the “Keplerian” portion of the curve, which are particularly well represented in the data in the negative direction as plotted in Fig. 5, returned to zero much more slowly than the data. An acceptable fit to the zero-offset positions could be obtained by assuming that the ellipticity of the isophotes did not represent the inclination angle of the gas disk. A much higher inclination near  $75^\circ$  was required in that case, and no corresponding fit to the offset positions at  $+0''.2$  and  $-0''.2$  could

be produced. The velocity amplitudes at the point of slit closest approach to the nucleus were very much higher than observed and the shapes were not at all congruent.

This result led us to question whether the abrupt isophote twist in the inner arcsecond actually represented the major axis of the gas disk. An alternative approach is to assume that the major axis of the larger scale emission-line structure defines the P.A. of the kinematic major axis of the inner gas disk. Baum et al. (1988) measured that angle on the larger scale to be  $83^\circ$ . That direction is nearly perpendicular to the measured P.A.'s of the radio jets of 3C 272.1, which are  $-5^\circ$  and  $+170^\circ$  (Laing & Bridle 1987). That choice fixes the relative slit angle at  $21^\circ$ . The free parameters are then the central mass and inclination angle. The best fit model is plotted over the data in Fig. 5, while its parameters (with uncertainty ranges) are given in Table 1. Fig. 5 shows reasonable agreement with the velocity amplitude and Keplerian shape for the zero-offset curves, and qualitative correspondence with the off-nuclear curves. Our Keplerian disk model fits the data very well, although there may be minor non-disk contributors to the emission-line profile (as suggested by the complexities of the inner emission-line isophotes [Paper I] and spectral profiles [Fig. 4]).

The acceptable range of the model parameters should be determined quantitatively. However, a proper derivation of  $\chi^2$  per degree of freedom is complicated by two factors: the data from adjacent pixels are strongly correlated through the PSF, and the uncertainties in velocity points are dominated by systematic effects in disentangling the multiple broad components. In addition, the derived central mass and disk inclination angle are themselves correlated. As the disk becomes more edge-on, the observed radial velocities more nearly represent the total velocity, implying a smaller mass for a given amplitude. That effect is overwhelmed by a competing effect in a thin disk model, which is the foreshortening in the transverse direction. A given pixel samples to much larger radii as the disk becomes edge-on, requiring larger mass to produce a given velocity amplitude. Increasing inclination angle therefore requires increasing mass. To set bounds on the acceptable range of mass, we sampled the two corners of the error ellipse. These represent approximately factors of 2 increase in  $\chi^2$ , but we did not attempt to optimize a data weighting scheme that fairly represented the systematic uncertainties. We did move to inclination angles that produced just discernibly poorer fits to the velocity curves, then varied the central mass to depart from the velocity amplitude by about  $1 \sigma$  at each extremum. A more realistic disk model with finite thickness would project more low radial velocity component into a given pixel, suggesting that the mass estimated from a thin disk is systematically too low.

How much of this nuclear mass can be attributed to luminous mass at the nucleus? The WFPC2 continuum images in Paper I show a bright nuclear point source with  $V = 19^m9$  (i.e.,  $L_V = 4.3 \times 10^6 L_\odot$  if  $A_V$  to the nucleus is  $0^m54$ ; Paper I) surrounded by the outer



stellar distribution. Is the emission from this continuum point source stellar or non-stellar? Additional spectroscopic observations of M84 are needed to address this issue. If we assume that the emission arises entirely from a stellar population with  $M/L_V \approx 5$ , the upper limit on the luminous mass at the nucleus is  $M_* \leq 2 \times 10^7 M_\odot$ . This is much less than the nuclear mass  $\approx 1.5 \times 10^9 M_\odot$  required to explain the gas disk dynamics (even given the uncertainty in the extinction). Thus, M84 contains a dark compact mass (most likely a BH given the presence of powerful radio jets).

Although it was surprising that the emission-line isophotes did not describe the geometry of the inner gas disk, the resulting picture is consistent with physical expectations. The angular momentum axis of the disk is now aligned with the axes of the dual radio jets. A gas disk nearly perpendicular to the plane of the sky would suggest that these bipolar radio jets are nearly in the plane of the sky, consistent with the roughly comparable power in the jets and lobes on either side of the nucleus. The more extended emission-line structure can now represent a natural source of gas for an inner accretion region, without the need for a strong, abrupt warp at  $\sim 40$  pc from the center.

The BH mass estimate of  $1.5 \times 10^9 M_\odot$  can be compared with the expectation from Kormendy & Richstone’s (1995) correlation between black hole mass and bulge mass. An update to that relationship by Kormendy et al. (1997) including 12 BH mass determinations predicts that the BH mass will be  $0.0022^{+0.0014}_{-0.0009} \times$  the bulge mass. For the total mass of M84, we use the structural parameter estimate of Bender, Burstein, & Faber (1992) of  $M = 5G^{-1}\sigma_0^2 r_e$ . We adopt their value of effective radius (scaled to a distance of 17 Mpc) of 4.5 kpc, and a central velocity dispersion of  $\sim 310$  km s $^{-1}$  from Davies & Birkinshaw (1988). The resulting total galaxy mass is  $5.1 \times 10^{11} M_\odot$ , with a predicted BH mass of  $1.1 \times 10^9 M_\odot$  within a range of  $(0.7 - 1.8) \times 10^9 M_\odot$ . Our best fit value of  $1.5 \times 10^9 M_\odot$  is very close to the ridge line of the Kormendy et al. correlation. At an  $M_B = -21.0$ , M84 is similar to M87 in total absolute magnitude (therefore, total implied mass) and central BH mass.

Our measurement of the BH mass in M84 (when combined with those for M87 and NGC 4261; see §1) has interesting implications for the physics of radio galaxies. A comparison of these three measured BH masses with the total radio luminosities of their associated radio sources (e.g., Roberts et al. 1991) suggests tentatively that these two quantities might not be directly correlated.

Several interpretive loose ends make M84 a galaxy meriting continuing study. The shapes of the inner isophotes are not now explained straightforwardly as a manifestation of an inner accretion disk. What produces the change in apparent P.A. and ellipticity? Are there unresolved near-nuclear H II regions that add to the complexity of the structure? Is there any relation between the sharp change in direction of the central dust lanes at  $\sim 100$

pc from the nucleus, as noted by Jaffe et al. (1994) and in Paper I, and the dynamical environment produced by the central BH? Although the best fitting systemic velocity for the gas disk is consistent with the systemic velocity of the outer filamentary gas derived from the two offset = 0'0 spectra, it is  $\sim 60 \text{ km s}^{-1}$  higher than the measured velocity for the stars (e.g., Davies & Birkinshaw 1988). Stiavelli & Setti (1993) noted that galaxies with a high contrast central potential could produce gravitational redshifts between central and outer samplings of the stellar velocity field of several tens of  $\text{km s}^{-1}$  in extreme cases. They found a  $1.4\sigma$  effect in the Davies & Birkinshaw measurements of the stellar field. If the dust lane obscuration of the central stellar light is significant, it is possible that the emission from the gas within 50 pc of the nucleus is coming from much deeper in the central potential well, accounting for some of the discrepancy. Resolution of this velocity difference is necessary to add confidence to the interpretation of the gas motion as that of a Keplerian disk around a large unseen mass at the dynamical center of M84.

We acknowledge useful comments from Eric Emsellem and the referee Ralf Bender and the assistance of P. Hall and C. Liu in planning these observations. Support for this work was provided to the STIS Investigation Definition Team by NASA.

## References

- Baum, S., et al. 1996, STIS Instrument Handbook, Version 1.0 (Baltimore: STScI)
- Baum, S. A., et al. 1988, *ApJS*, 68, 643
- Baum, S. A., Heckman, T., & van Breugel, W. 1990, *ApJS*, 74, 389
- Baum, S. A., Heckman, T., & van Breugel, W. 1992, *ApJ*, 389, 208
- Bender, R., Burstein, D., & Faber, S. M. 1992, *ApJ*, 399, 462
- Bower, G. A., Heckman, T. M., Wilson, A. S., & Richstone, D. O. 1997, *ApJ*, 483, L33  
(Paper I)
- Burstein, D., & Heiles, C. 1984, *ApJS*, 54, 33
- Davies, R. L., & Birkinshaw, M. 1988, *ApJS*, 68, 409
- Fanaroff, B. L., & Riley, J. M. 1974, *MNRAS*, 167, 31P
- Ferrarese, L., Ford, H. C., & Jaffe, W. 1996, *ApJ*, 470, 444
- Hansen, L., Nørgaard-Nielsen, H. U., & Jørgensen, H. E. 1985, *A&A*, 149, 442
- Harms, R. J., et al. 1994, *ApJ*, 435, L35
- Jaffe, W., et al. 1994, *AJ*, 108, 1567
- Jones, D. L., Sramek, R. A., & Terzian, Y. 1981, *ApJ*, 246, 28
- Kormendy, J., Bender, R., Evans, A. S., & Richstone, D. 1997, *AJ*, submitted
- Kormendy, J., & Richstone, D. 1995, *ARA&A*, 33, 581
- Kormendy, J., et al. 1996, *ApJ*, 459, L57
- Laing, R. A., & Bridle, A. H. 1987, *MNRAS*, 228, 557
- Mould, J., et al. 1995, *ApJ*, 449, 413
- Roberts, M. S., Hogg, D. E., Bregman, J. N., Forman, W. R., & Jones, C. 1991, *ApJS*, 75,  
751
- Stiavelli, M., & Setti, G. 1993, *MNRAS*, 262, L51

Fig. 1.— Our STIS slit positions (with the solid lines representing the slit edges) superposed on Paper I’s  $H\alpha + [\text{N II}]$  image, which is displayed here with a logarithmic stretch with a range in intensity covering a factor of 100.

Fig. 2.— A magnified view of the last offset =  $0''.0$  spectrum centered on the  $[\text{N II}] \lambda 6583$  emission line. To emphasize the velocity gradient, the continuum distribution has been subtracted, and the intensity scaling is logarithmic. The color scale maps the range of velocity along the slit, with blue and red color representing velocities with respect to systemic that are blueshifted and redshifted, respectively. The dispersion axis (horizontal) covers a velocity interval of  $1445 \text{ km s}^{-1}$ , while the spatial axis (vertical) covers the central  $3''$ .

Fig. 3.— Plots of the three spectral rows bracketing the nucleus from the last spectrum obtained (offset =  $0''.0$ ). The distance along the slit  $R$  is given in each panel, and the dashed lines represent the systemic velocity of the  $[\text{N II}] \lambda 6583$  and  $[\text{S II}] \lambda 6731$  emission lines.

Fig. 4.— Profiles of the  $[\text{N II}] \lambda 6583$  emission line at positions within  $\sim 0''.3$  of M84’s nucleus. The spectra have been continuum subtracted and normalized to the peak intensity of  $[\text{N II}] \lambda 6583$ . For each of the four slit positions, the offset from the nucleus is given along the bottom, where negative values of the offset move the slit toward P.A. =  $14^\circ$  on the sky. The position along the slit (relative to the nucleus) in arcseconds is shown on the left, where increasing values are toward P.A. =  $104^\circ$ . Each profile covers a heliocentric velocity range of  $200 - 2200 \text{ km s}^{-1}$ , and the systemic velocity is indicated by a dashed line. All profiles were taken from a single row in the data, except for the profiles at  $+0''.30$  along the slit which were binned by 4 pixels =  $0''.2$  to improve the S/N.

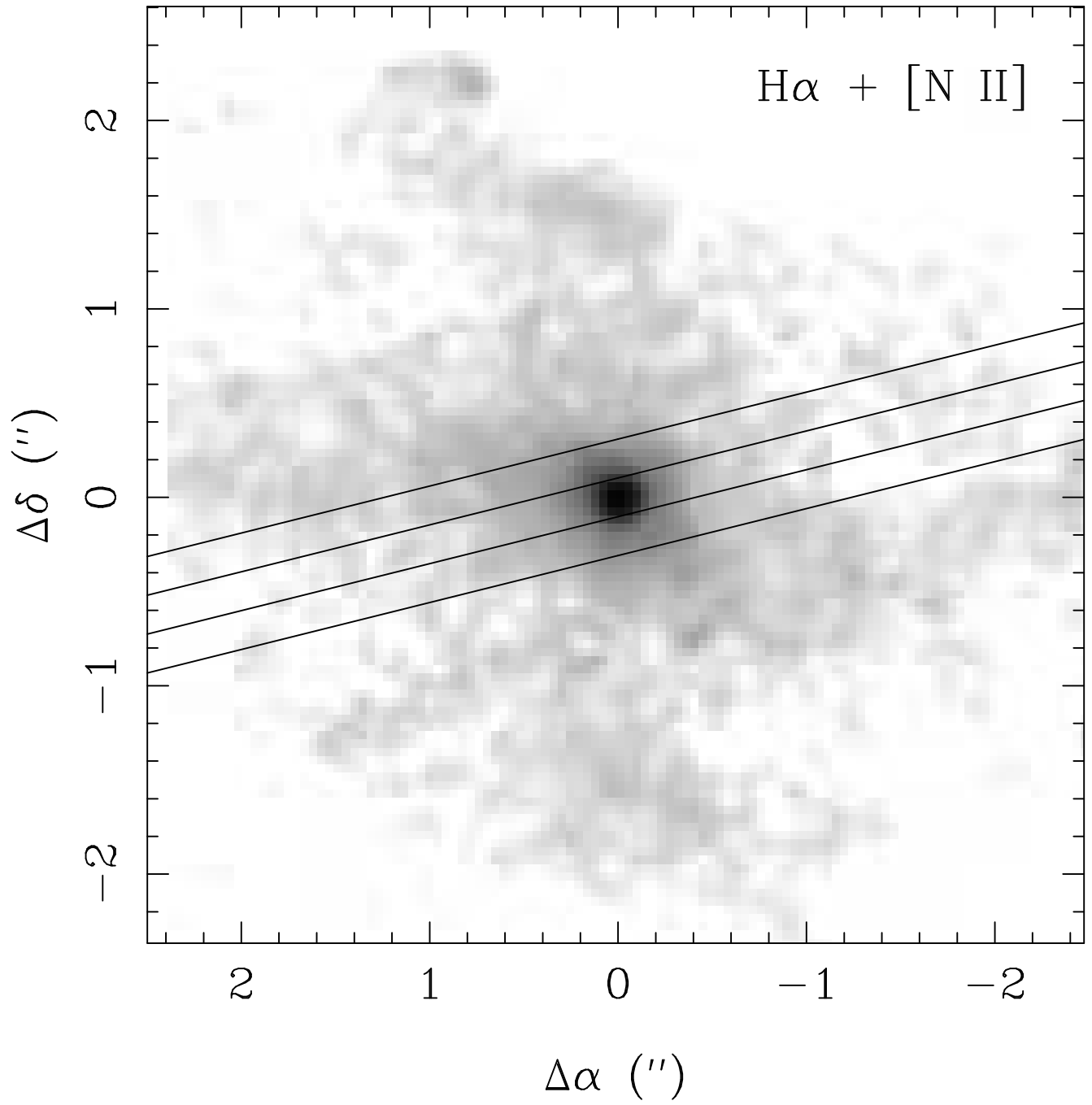
Fig. 5.— The heliocentric velocity as a function of distance along the slit for each slit position. Crosses indicate velocities measured by the cross correlation technique described in the text. Closer to the nucleus where two kinematic components are present, open triangles represent the low-velocity component, and filled circles or squares represent the high-velocity component. The squares denote positions where the high-velocity and low-velocity components cannot be separated because both are at or near the systemic velocity. The errors in the data points are  $\leq 25 \text{ km s}^{-1}$  (i.e., no larger than the size of the points). The velocities predicted by the best fit thin Keplerian disk model are represented by open circles connected by a solid line.

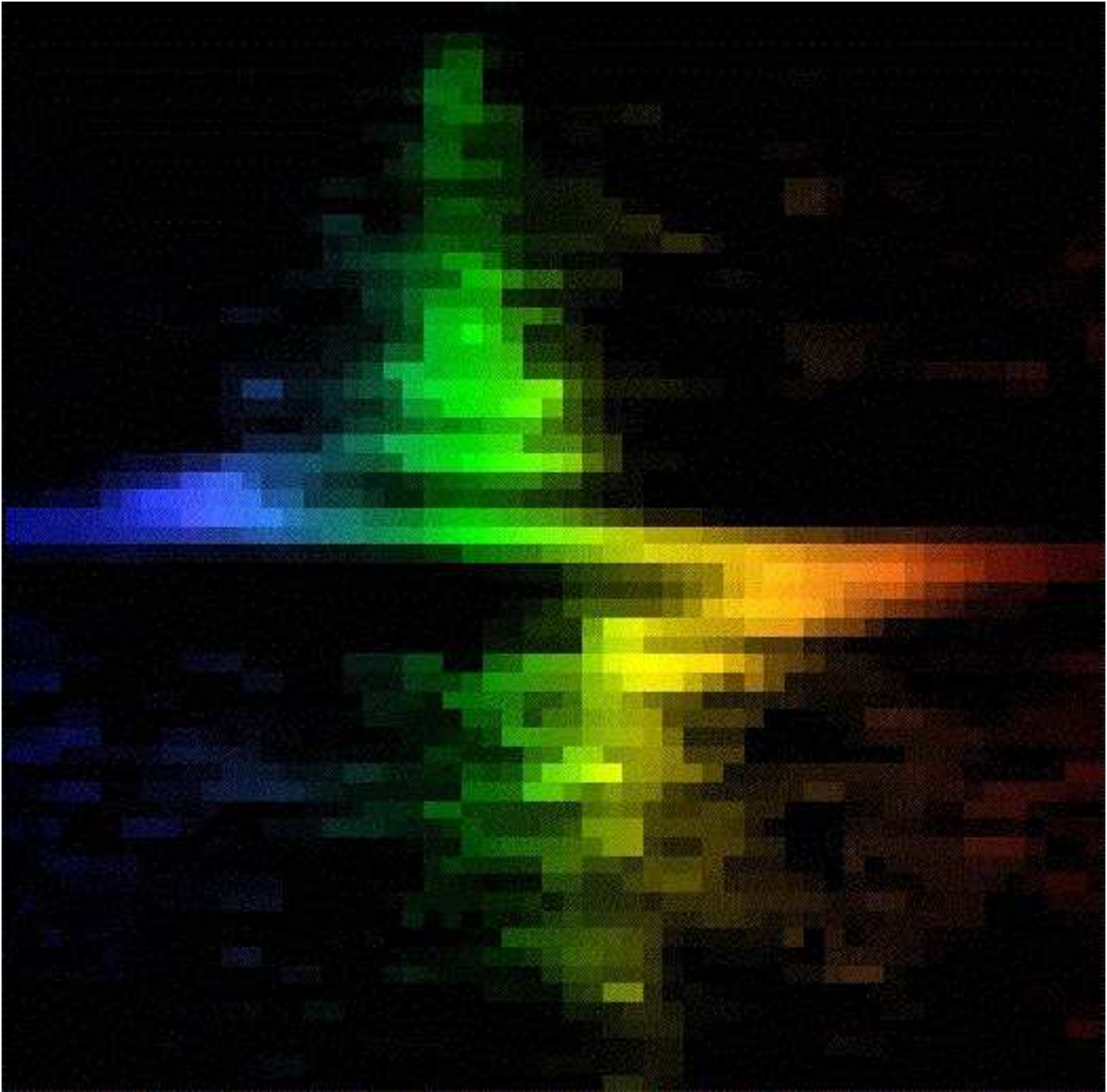
Table 1. Keplerian Disk Model Parameters

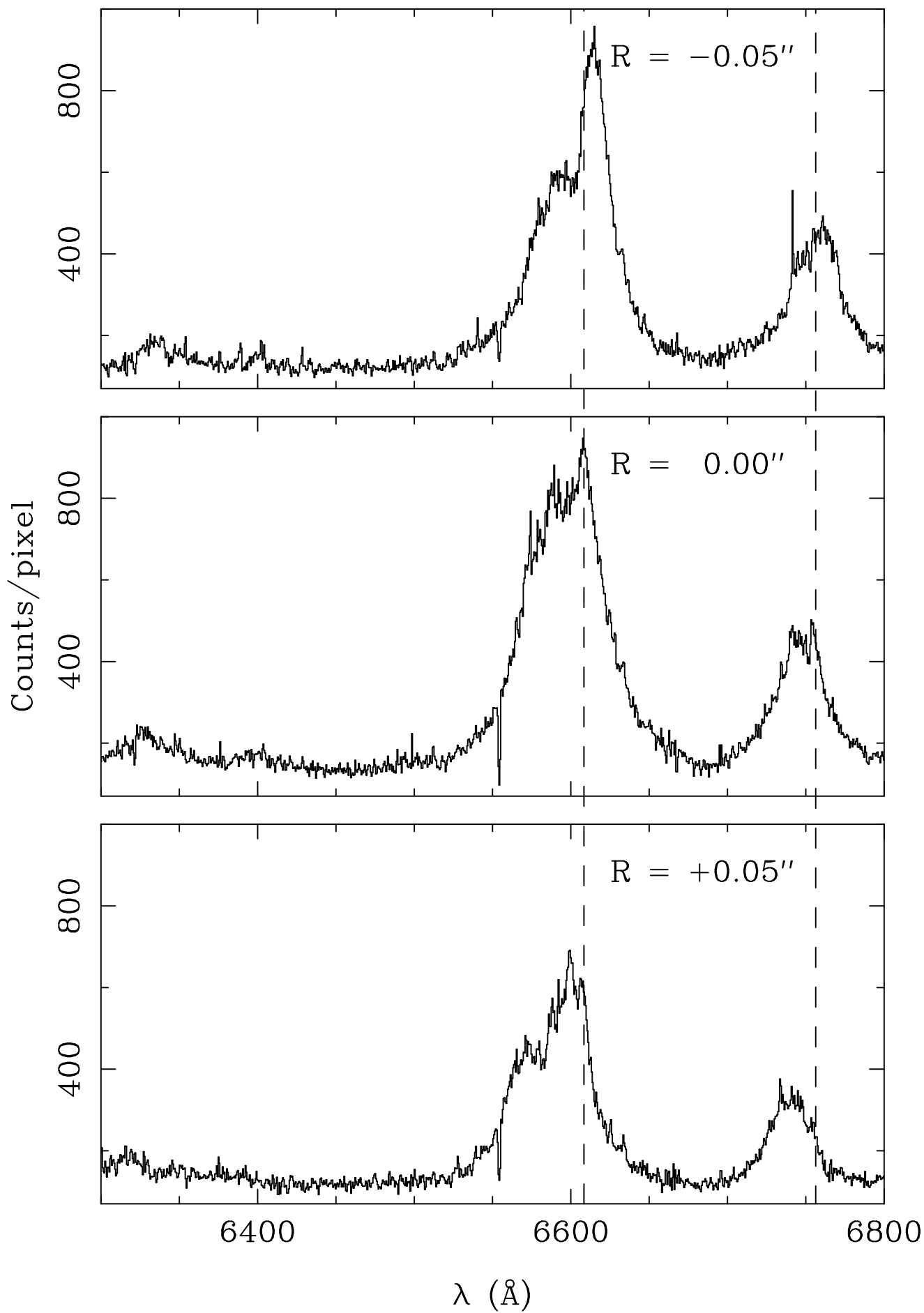
Parameter	Best Fit	Uncertainty Range
Black Hole Mass ( $M_{\odot}$ )	$1.5 \times 10^9$	$(0.9 - 2.6) \times 10^9$
Disk Inclination ( $^{\circ}$ )	80	75 – 85 <sup>a</sup>
Disk P.A. ( $^{\circ}$ )	83	80 – 85
Gas systemic velocity ( $\text{km s}^{-1}$ )	1125	1100 – 1150
Intensity law	$I(r) \propto r^{-1}$	
$I(r)$ inner radius (pc)	1	0.3 – 3
$V(r)$ inner radius (pc)	0.03	0.01 – 0.1
PSF $\sigma$ ( $''$ )	0.05	0.04 – 0.06

<sup>a</sup>Lower mass requires lower inclination

M84

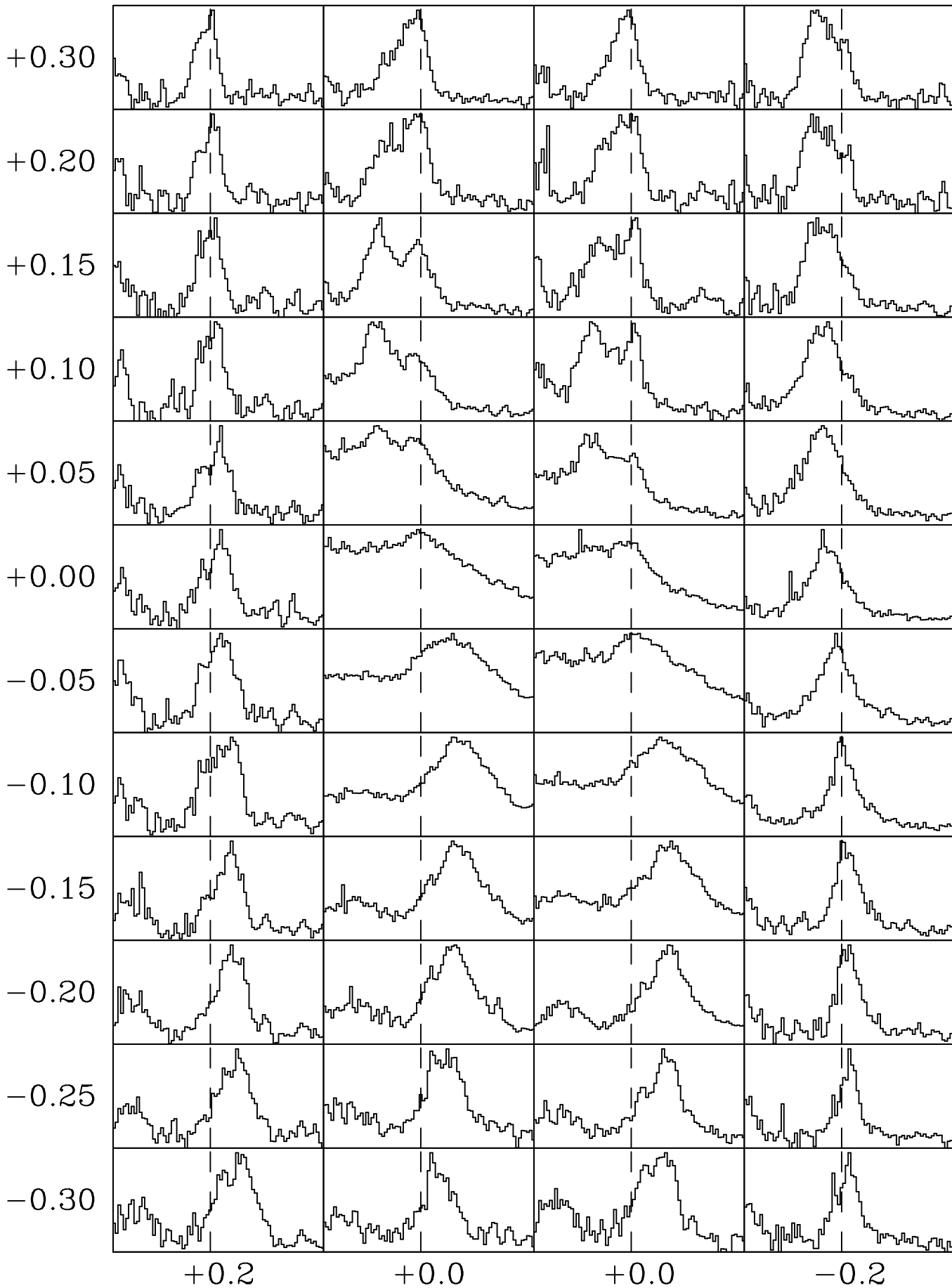








2000 km s<sup>-1</sup>



↑  
PA = 104°

offset (")

